PHYSICAL REVIEW E VOLUME 59, NUMBER 4 APRIL 1999

Morphology transitions in diffusion- and kinetics-limited solidification of a liquid crystal

Jeffrey L. Hutter* and John Bechhoefer
Department of Physics, Simon Fraser University, Burnaby, British Columbia, Canada V5A 1S6

(Received 16 June 1998; revised manuscript received 7 December 1998)

A single material can solidify into a variety of macroscopic morphologies depending on the undercooling. The manner in which one morphology changes into another as the undercooling is varied has received inadequate experimental attention, particularly for cases where the undercooling is large. There are two main possibilities: there can be distinct transitions, in analogy with equilibrium phase transitions, or there can be a continuous crossover, where one morphology gradually transforms into the next. We have studied the isothermal crystallization of the liquid crystal 10 OCB from its smectic-*A* phase. As the undercooling is varied, we see several sharp transitions in the growth structure, accompanied by singular points in the front velocity curve. We identify three types of morphology transitions: strongly first order, where the front velocity is discontinuous; weakly first order, where the velocity curve, but not its derivative, is continuous (and the morphology changes discontinuously); and second order, which shows pretransitional effects and continuous changes in growth properties. [S1063-651X(99)04104-5]

PACS number(s): 81.10.Aj, 64.70.Md, 81.30.Fb

I. INTRODUCTION

During solidification, the existence of a nucleation barrier causes growth of separate domains with well-defined fronts, rather than simultaneous freezing throughout the entire sample. The nature of such a growth front depends on growth conditions and, in turn, determines the structure and properties of the resulting solid.

One important parameter is the undercooling ΔT, the amount of cooling below the equilibrium phase coexistence temperature. For $\Delta T < L/c$, the latent heat L released by freezing is enough to raise the local temperature above the melting point (c is the heat capacity). Solidification can then proceed only if this heat is removed from the vicinity of the front. Typically, diffusion is the dominant transport mechanism and the growth is known as *diffusion-limited* growth. In the diffusive regime, the well-known Mullins-Sekerka instability [1] can cause a flat interface to become unstable, leading to forms such as dendritic growth.

For $\Delta T > L/c$, heat transport is no longer required and attachment kinetics at the interface become the rate-determining step. The diffusive instability is then removed, but, in practice, a flat interface is rarely seen. Instead, a variety of phenomena including defect generation, polycrystalline solids, metastable phases, and, at the highest undercoolings, glass formation, are seen.

The variation of growth properties with growth conditions has been modeled in several systems. For instance, the tip velocities and curvatures of dendrites vary continuously with undercooling [2]. In the kinetic regime, changes in growth forms of polymers [3] and metal alloys [4] have been modeled as a gradual crossover between growth limited by surface nucleation and growth limited by lateral spreading of the surface steps (i.e., ''regime theory'').

More recently, sharper transitions between morphologies have been examined, particularly in the diffusive regime [5–11]. Nondendritic morphologies such as the dense-branched morphology have been seen in experimental and numerical models under conditions where dendritic solutions are known to exist [6,11,12]. This suggests that a selection rule between distinct morphologies (each of which has its own dependence on growth conditions) is at work. These models, as well as theoretical discussions, show that the transitions between morphologies can be sharp. The question then becomes: Can one determine which of the available growth morphologies is seen?

A long-time goal in nonequilibrium physics has been to formulate the problem of pattern selection (i.e., in this case, growth morphologies) in terms of an extremum principle analagous to the minimization of a free energy in equilibrium thermodynamics. Despite intensive effort, no general kinetic potential for nonequilibrium systems has been found, though specialized approaches have proven useful in specific cases [13]. It is possible that such a potential involving *local* (in space and time) growth properties cannot be found — the growth form may depend on the growth history, as well as on current growth conditions.

In some cases, however, it has been possible to divide the space of growth parameters into a phase diagram [5,6,11,12]. Ben-Jacob and co-workers [12] have discussed morphology transitions and selection principles in terms of the average growth velocity, which can be thought of as a response function to the driving force in the system (e.g., the undercooling, supersaturation, etc.) [6]. Since the rate of change in free energy at the interface is given by the integral of velocity along the interface, the appropriate average must take interfacial shape into account. They define two types of morphology transition in analogy with equilibrium phase transitions: first order, in which the velocity (as a function of a growth parameter such as undercooling) is discontinuous at the transition point, and second order, in which the velocity, but not its derivative, is continuous.

An intuitively appealing selection principle is that the fastest growing morphology is the one dynamically selected because it outruns competing growth modes, eventually surrounding them and preventing further growth. It should be

---

*Present address: Exxon Research and Engineering Company, Route 22 East, Annandale, NJ 08801.

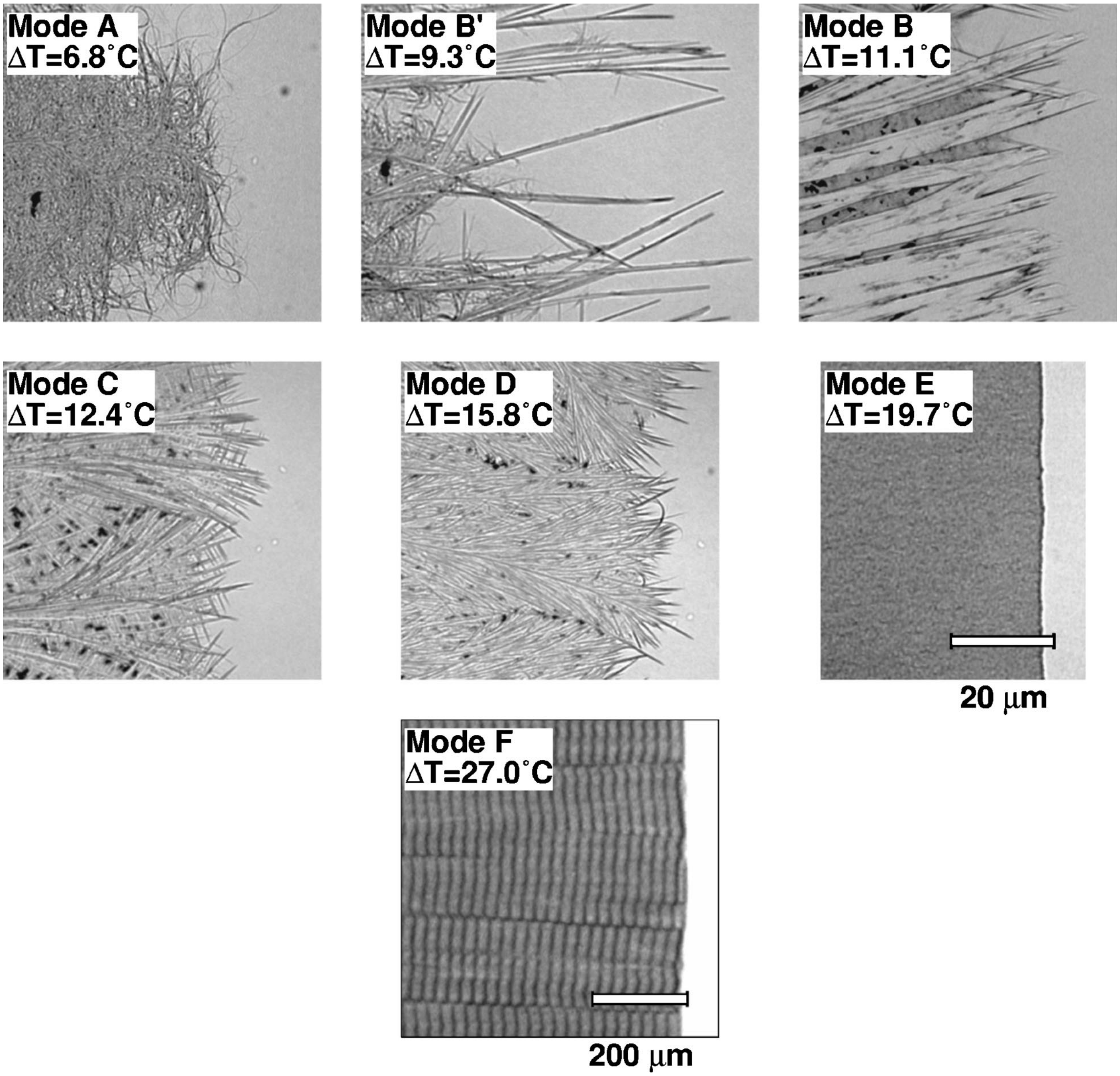

FIG. 1. Micrographs of 10 OCB solidification fronts. Each is the result of a separate experiment performed at the indicated undercooling. In the order of increasing undercooling, we see mode *A*, growth in the form of tangled fibers; mode B', long needles traveling ahead of a front that resembles mode *A*; mode *B*, thick faceted needle crystals; mode *C*, dendritic growth with side branching; mode *D*, growth superficially similar to mode *C*, but with branching at noncrystallographic angles and tips that are often bent; mode *E*, spherulitic growth with a smooth front made up of crystals too small to see optically; mode *F*, banded spherulitic growth. Growth is to the right in all cases. Note that the scale of image *F* differs from that of A–E.

noted that the fastest-growing mode hypothesis cannot, on its own, describe the first-order transition defined above — in one direction, the transition *must* be to a slower mode. Ben-Jacob and co-workers suggest that, just as entropy dominates the equilibrium free energy at high temperature, the growth velocity, representing the rate of entropy production, may be the most important term far from equilibrium. A more general selection principle may also involve variables associated with the microscopic structure of the interface.

Morphology transitions have been observed in both experimental and computational work. In many cases, particularly in patterns observed in the Hele-Shaw cell and in simulations of diffusion-limited growth, the fastest-growing mode hypothesis holds [6]. Other clear examples have been seen in the measurement of growth velocities in metal alloys [9]. However, we are aware of one counterexample in the literature: measurements of growth velocities in pure nickel and copper-nickel alloys show an apparent morphology transition associated with a *decrease* in the slope of the velocity curve — i.e., to a slower mode [8]. In this case, the relevance to morphology transition schemes was not discussed.

There are few examples in the literature in which the variation in growth morphology (let alone the velocity, which is often not measured at all) has been characterized well enough to distinguish between continuous and sharp transitions, particularly in the kinetic regime. In a recently published paper [14], we presented accurate measurements of growth velocities along with measurements of front mor-

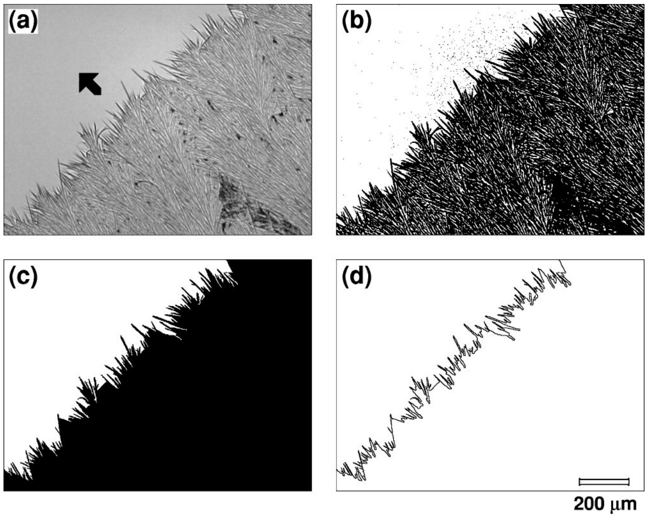

FIG. 2. Measurement of the solidification front location. (a) Image of the solidification front. (b) Thresholded image differentiating between the solidified material (black) and the smectic *A* phase (white). (c) Image (b) with all points enclosed by the front set to black and all non-enclosed black points set to white to remove noise. (d) Pixels at the boundary between the phases.

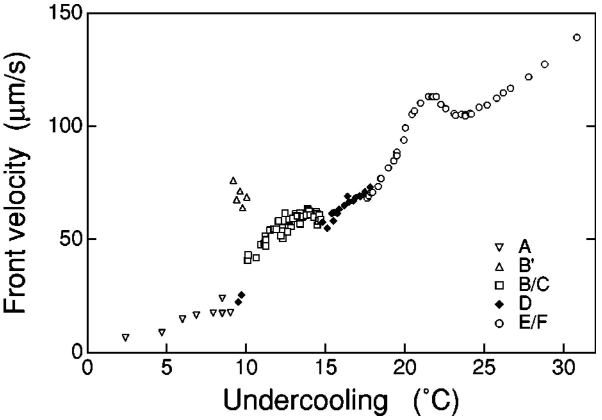

FIG. 3. Growth velocity of 10 OCB as a function of undercooling. Note that separate branches of this curve are marked by discontinuities in the slope and, in some cases, in the curve itself. The labels indicate the modes illustrated in Fig. 1. The data points at small undercoolings were measured using a camera lens in place of the microscope to provide larger-scale averages for the rougher fronts.

phology for a single-component system. Here, we give a full account of our work and discuss each transition seen.

II. EXPERIMENT

We selected the liquid crystalline material 4-cyano-4′-decyloxybiphenyl (10 OCB) for our solidification study [15]. 10 OCB exhibits a series of distinct solidification morphologies as the undercooling is varied. The main reason for this choice of material is one of convenience: morphology transitions occur at velocities useful for video microscopy (10–100 μm/s) and the material is easily undercooled, allowing studies of growth in the kinetic regime. In contrast, interesting behavior in polymer crystallization often occurs at velocities less than 1 μm/s, while metals solidify with front velocities of meters per second [16]. Nevertheless, many of the growth modes observed are also seen in other systems, making 10 OCB a useful model system.

The samples consisted of a thin (10 μm) layer of 10 OCB sandwiched between two glass plates. Thin (~170 μm) plates were used to ensure rapid cooling to the desired temperature. A complication of using a liquid crystal is that solidification occurs from a supercooled liquid crystal phase rather than from the supercooled, isotropic melt. In order to create a defect-free sample with isotropic properties in the two-dimensional plane of the layer, the glass plates were treated with an organosilane [17] to impose homeotropic anchoring with smectic layers parallel to the surfaces.

In a typical solidification experiment, we begin by melting the sample into the isotropic phase on a hot plate. We then transfer the sample quickly to a computer-controlled hot stage [18] set to the desired undercooling (typical stability was 10 mK, with maximum gradients of 10 mK/mm). The sample quickly enters a supercooled smectic phase. As most of the experiments are performed between 20 and 50 °C, the perturbation to the oven temperature due to inserting the hot sample is usually small enough that the oven returns to its initial temperature before nucleation of the solid phase.

We studied the solidification front using optical microscopy [19]. Sequences were stored digitally using a charge coupled device (CCD) video camera [20] and frame grabber [21]. In some cases, the field of view of the microscope was too small to adequately estimate the direction and magnitude of the solidification velocity. This typically occurred at small undercoolings, where the growth front becomes very rough. For these experiments, we used a video lens [22], rather than the microscope.

Figure 1 illustrates the growth morphologies seen over the range of undercooling studied. Several of these growth modes are similar to growth seen in other materials. For instance, dendrites (mode *C*) are characteristic of diffusion-limited growth in inorganic salts, organic solids, and metals. Spherulites (modes *E* and *F*) are important in the solidification of many materials, notably polymers [23]. Other modes, such as the tangled whiskers of mode *A* and the noncrystallographically branched bundles of mode *D* are less familiar.

In order to characterize quantitatively the modes and their transitions, we have measured properties of the growth front. This required that curves indicating the locations of the fronts be extracted from pictures such as those in Fig. 1. We accomplished this using the procedure outlined in Fig. 2 [24]: The image is thresholded so that the solid region (which is darker due to scattering from the polycrystalline solid phase) is predominantly black. (Low-contrast images sometimes required a prior background subtraction to remove illumination variation across the sample.) All points enclosed by the front are set to black [cf. Fig. 2(c)] to remove noise in both phases. The front is then defined to be the set of black points which border at least one white point and is tabulated as an (unordered) set of x_i, y_i coordinates.

Note that in some cases, pockets of unsolidified material may be present behind the front defined in this manner. For our purposes, the average properties of the front defined above are sufficient to distinguish the growth morphologies. However, the structure behind the front is important in identifying the growth as either diffusion- or kinetics-limited

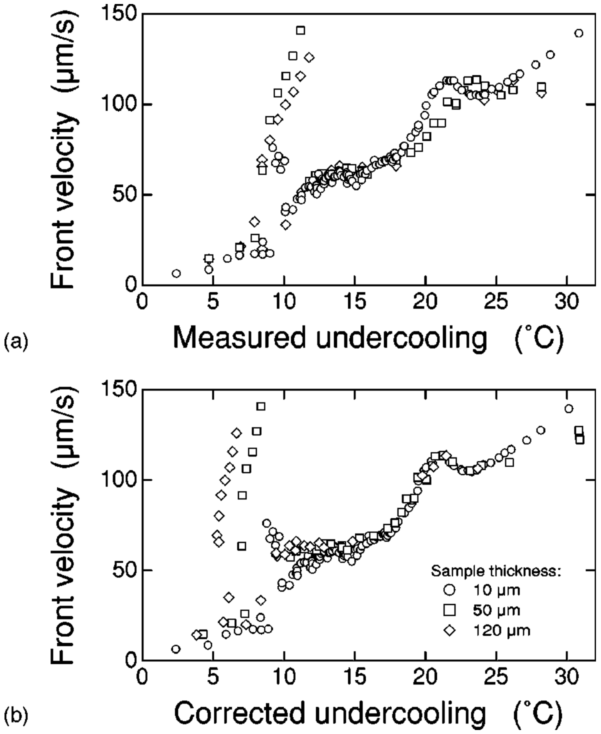

FIG. 4. Effect of thickness on the front temperature. (a) Velocity data for three sample thicknesses. (b) Data from (a) corrected to account for reheating due to the generation of latent heat. A thermal diffusion constant of 1.25×10^{-3} cm^2/s was assumed.

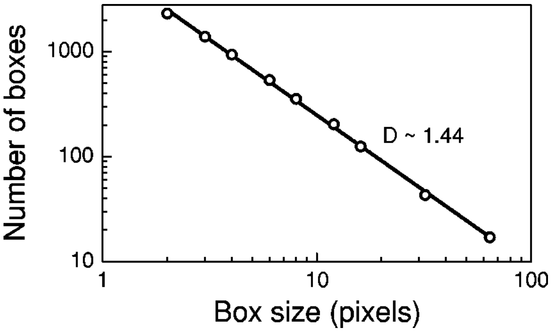

FIG. 5. Measurement of the fractal dimension. A log-log plot of the number of boxes required to cover the interface vs box size can be used to estimate the fractal dimension of the interface. The slope of the straight line indicates that the growth front has a fractal dimension of ~1.4 over the length scales measured in the image. The interface used in this example is shown in Fig. 2.

growth. In general, the latent heat released from the interface in diffusion-limited growth in an infinite three-dimension system (or quasi-two-dimensional system with insulating side walls) produces an open structure whose fraction of solidified material is proportional to the undercooling. In our system, heat transfer through the sides of the thin sample allows this structure to eventually fill in, so identification of diffusive growth must be based on the structure very near the front. This additional mechanism of heat diffusion allows the kinetics-limited regime to be more easily reached. The open structures of modes A–D identifies them as diffusion-limited growth modes [25].

Once the set of pixels comprising the front has been determined, its change in position over time can be used to determine the front velocity. We fit a circular arc to each set of interface points and measured the velocity from a plot of arc radius versus time. In practice, the centers of the best-fit arcs depended on the range of points used for the fits and were quite different for different frames of the sequence. To deal with this, we forced the centers for the entire sequence to lie at the average center for a first set of fits. In addition, it was necessary to first rotate the fronts so that they were roughly along the x axis. This largely eliminated problems associated with the uncertainty in x_i: when the derivative dy/dx of the arc is large, a small change in x_i can result in a large change in the χ^2 value, which measures the vertical deviation from the fitting function, rather than the perpendicular deviation that would be more appropriate here.

Using these techniques, we constructed the velocity curve shown in Fig. 3. Each point in this plot represents a separate experiment using the same (remelted) sample. The modes from Fig. 1 corresponding to different regions of this plot are indicated. Note that the boundaries between modes are the points where the velocity curve or its derivative is discontinuous. This claim will be further justified in the following section.

Since the velocity versus undercooling curve is an important element of this study, we require accurate measurements of the local interface temperature. This temperature is higher than that of the heat bath due to latent heat released by the solidification front. The thin-cell geometry allows this latent heat to be removed through the glass walls of the sample cell, rather than through the sample itself, resulting in a steady state with a constant front temperature and velocity. We investigated this temperature rise at the interface by varying the sample thickness. Figure 4(a) shows the velocity data for three sample thicknesses. Heat loss through the sample walls is slower for thicker samples, resulting in a higher front temperature and, hence, a smaller undercooling. The result is velocity curves that are progressively stretched along the undercooling axis as the apparent undercooling (as measured by the oven temperature) becomes progressively larger than the true undercooling.

We estimate the temperature rise for a flat interface propagating at constant velocity into an infinite thermally conducting medium as [26]

$$\delta T = -\frac{Lvd}{2\pi D\rho c}\ln\frac{vd}{4\pi D},$$

where L is the latent heat per unit volume of sample, v is the front velocity, d is the sample thickness, and D, ρ, and c are the thermal diffusion constant, mass density, and specific heat capacity at constant volume per unit mass, respectively, of the conducting medium (taken here to be the glass plates since the contribution of the thin sample is negligible). The result of applying a correction of this form to the data of Fig. 4(a) is shown in Fig. 4(b). Note the marked improvement in the overlap of the three curves through most of their range. The poor results at small undercooling are expected — in this region our fronts are far from flat and the assumption of a line interface and effectively infinite medium break down. Since we mainly used sample thicknesses of ~10 μm, where the predicted temperature correction is only ~0.6 °C

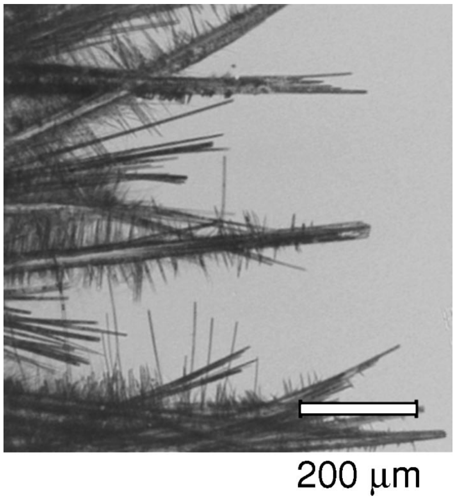

FIG. 6. Mode B' needles in a thick cell (thickness=120 μm,$\Delta T = 9.4\,°\mathrm{C}$.)

at $v = 100$ μm/s, and since no correction is available for the rough fronts, we chose to display uncorrected data.

Two measures of the front morphology are the roughness and the fractal dimension. We used the root-mean-square deviations of the data points from a fit to the interface to measure roughness. Although the location of the center of the circular arcs used for the velocity measurement had little effect on the velocity estimate, it did have a large effect on this roughness measurement. For this reason, we chose to measure RMS deviations from individual quadratic fits to each set of data. This had the effect of neglecting the contribution of roughness on length scales comparable to the image size. We estimated the fractal dimension using a box-counting algorithm [27]. We find that this measurement provides values of the fractal dimension that are constant at length scales over a range of almost two orders of magnitude (Fig. 5).

Neither of these measurements provides a complete description of the growth front. Moreover, the roughness measure, as has been pointed out, was limited to the high-frequency components. Nevertheless, we will see that these quantities can provide very clear signals of sudden *changes* in the growth morphology.

III. SMOOTH-CROSSOVER TRANSITIONS

So far, we have discussed growth morphologies and mode transitions without a careful definition of terms. We will define the *growth morphology* as the structure of the solid phase *near* the growth front. In principle, this need not be the equilibrium structure that will be seen long after solidification. In practice, the growth structure persists for at least many days. The term *growth mode* will refer to a distinct morphology separated from those seen under different growth conditions by fairly rapid changes in morphology. We will be most interested in cases where sharp changes occur: *morphology transitions*. Once we have admitted the possibility of sharp transitions, we may then ask what principle selects one competing morphology over another.

Not all transitions need be sharp. Modes B and C shown in Fig. 1 are apparently quite different. Mode B exhibits large needles with faceted tips and few side branches, while mode C resembles classical dendrites with rounded tips and crystallographic sidebranching. However, the transition between these two modes appears to be smooth: no singularity in the velocity curve was ever seen (see Fig. 3), nor were sharp changes measured in any of the front properties as the undercooling was varied. Moreover, changing the undercooling *during* growth produced a gradual change that occurred simultaneously throughout the entire front. This case is in sharp contrast to the transitions between other modes seen in 10 OCB.

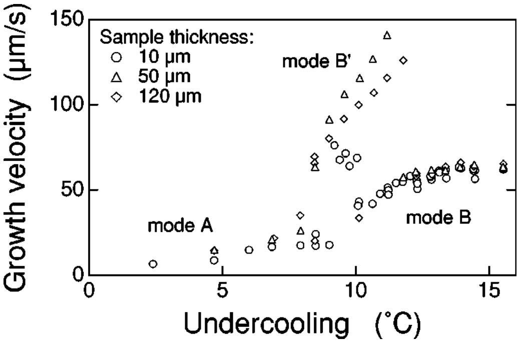

FIG. 7. Effect of sample thickness on mode-B' velocities. For thicknesses of 50 and 120 μm, mode B' grows at larger velocities and is observed over a wider range of undercooling than for samples of 10 μm thickness.

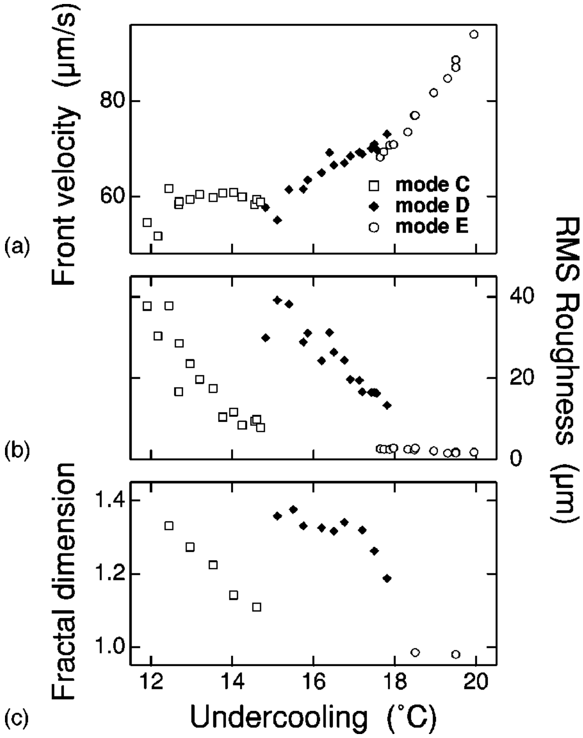

FIG. 8. Velocity and roughness data for modes C–E. The symbols for the data points indicate the growth morphology, as determined from microscope images. (a) Velocity as a function of undercooling. Note the sharp changes in slope near $\Delta T = 15\,°\mathrm{C}$ and $\Delta T = 18\,°\mathrm{C}$. (b) RMS roughness of the growth front. Note the sudden changes in roughness at the discontinuities in the velocity curve. (c) Fractal dimension. The sudden changes in growth form are also apparent in measures of the fractal dimension.

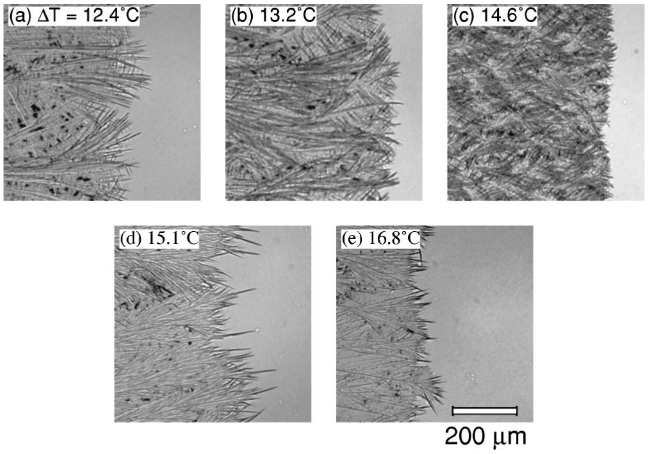

FIG. 9. Evolution of front morphology across the CD transition. (a)–(c) show the dendritic structure of mode C at increasing values of the undercooling. Note that the front roughness decreases from (a) to (c). In (d), a slightly larger undercooling has resulted in the mode-D structure, which itself becomes smoother in frame (e).

IV. STRONGLY FIRST-ORDER TRANSITIONS

The large jump in velocity clearly identifies the transitions involving mode B' [28] as first-order morphology transitions. Despite much effort, we were never able to produce growth velocities between modes B and B', suggesting that there is a true discontinuity. The sharp transition is also seen in measurements of quantities such as the average needle width: the mode B' needles are much narrower than those of mode B.

Since any transition *out* of mode B' is necessarily to a mode with a smaller growth velocity, the selection principle in this case must involve parameters other than the front velocity. One possibility is that the growth mechanism for B' can only exist over a small range of undercoolings. However, we would then expect to see evidence of a singularity in some of the growth properties as the end of the domain is reached. We find that the growth properties *within* mode B' growth vary smoothly with undercooling.

Another possibility is that there is a selection rule other than the ''fastest mode'' hypothesis at play. Ben-Jacob and co-workers have suggested that the general selection rule may involve an additional contribution related to the front structure. Our observations suggest that mode B', with its infrequent sidebranching (see Fig. 1, mode B'), lacks an effective mechanism for lateral spreading. Indeed, most of the solidified material far behind the envelope of advancing B' needles resembles mode A.

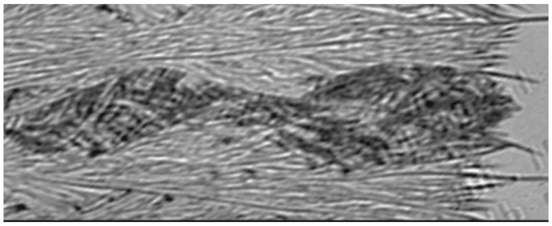

FIG. 10. The DC transition. The darker region is a portion of mode C that is in the process of spreading laterally at the expense of mode D. The figure spans 300×750 μm. Growth is to the right.

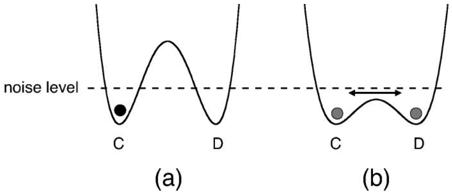

FIG. 11. Morphology hopping at coexistence. (a) A large barrier relative to the noise level will not allow a morphology transition during the finite time of the experiment. (b) Hops between morphologies are likely when the barrier height is comparable to the noise level.

We also note that the width of mode B' needles is similar to the sample thickness, suggesting that the sample geometry is important. To explore this idea further, we grew mode B' domains in thicker cells (50 and 100 μm). In such samples, the microcrystals became larger (Fig. 6) and the velocity discontinuity became more pronounced (Fig. 7).

Although the apparent undercooling range for mode B' is increased in thicker samples, it is not clear that the true range of undercooling has been increased. Latent heat is not conducted away from the growth front as efficiently for thick cells, so the true undercooling will be less than that set by the oven for quickly growing fronts (which have the largest rate of heat production). Although our focus is on morphologies appearing in the thin-cell geometry, it is interesting to note that the observations in thick cells suggest that mode B', with its large velocity discontinuity, will persist even for true three-dimensional growth.

V. WEAKLY FIRST-ORDER TRANSITIONS

In addition to the first-order AB' and $B'B$ transitions, sharp morphology transitions are seen between modes C and D, and between D and E. As shown in Fig. 8(a), the velocity curve is continuous at these transitions, but the slope of this curve is not. Referring to the nomenclature of Ben-Jacob and co-workers, we might label these as second-order morphology transitions. However, we will show that these are true first-order transitions, albeit with no detectable hysteresis in the velocity-undercooling curves.

We first consider the CD transition. Although the velocity curve is continuous, there is a sudden change in the structure, as shown by Figs. 8(b) and 8(c). The two modes are superficially similar (i.e., similar roughness and fractal dimension) near the centers of their respective undercooling ranges, but are quite distinct near the transition. This evolution of front structure can be clearly seen in Fig. 9.

Further evidence that the CD transition is first order is provided by the dynamics: if the undercooling of a growing mode-D front is changed to a value where mode C would normally be observed, the transition occurs by nucleation and lateral growth of mode C (and vice versa). This process is shown in Fig. 10, where a region of mode C has nucleated after a sudden decrease in undercooling.

Despite the need for the new mode to nucleate during the morphology transition, no hysteresis is seen in Fig. 8(a) — there is no region of overlap. This prompts us to term this transition *weakly* first order, in contrast to the strongly first-order AB' and $B'B$ transitions. The most stable mode is able

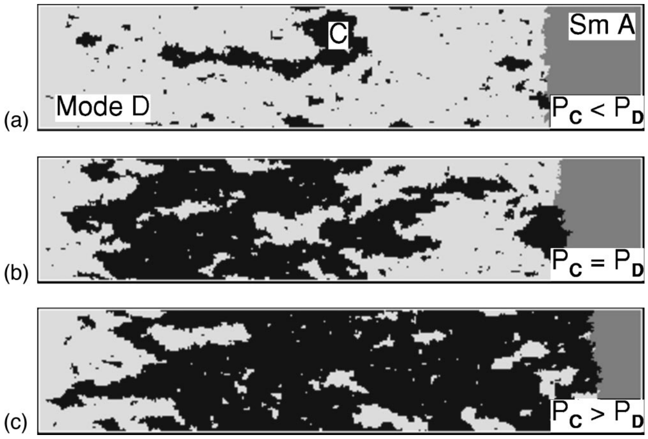

FIG. 12. Simulation of mode nucleation (100×500 lattice spacings). Three cases are shown: (a) Growth probabilities $P_C = 0.2$, $P_D = 0.207$, and $P_S = 10^{-3}$ (see text). The initial mode *D* (white) dominates. (b) $P_C = 0.2$, $P_D = 0.2$, and $P_S = 10^{-3}$. Domains of modes *C* and *D* alternate. (c) $P_C = 0.207$, $P_D = 0.2$, and $P_S = 10^{-3}$. Once it has nucleated, mode *C*, which now has the largest growth velocity is able to take over the growth front.

to consistently establish itself before the front arrives at the center of the cell, where it is recorded, regardless of the mode that nucleates initially, even when the undercooling is set near the transition point.

The general idea underlying our distinction between weakly and strongly first-order transitions is illustrated by considering a double-welled potential at coexistence (see Fig. 11). In Fig. 11(a), the noise is much less than the barrier height, so that there is little chance that the system, say in state *C*, will jump to *D* during the fixed, finite duration of the experiment. In Fig. 11(b), by contrast, the barrier height is comparable to the noise level and hops back and forth are likely. In this system, at other undercoolings, the relative hopping rates will be skewed towards the lower well, shifting the amounts of *C* and *D* correspondingly. Note that ''noise'' here does not refer to thermal noise, but is a measure of the randomness (due to the needle-shaped crystallites, nucleation, etc.) present in the microstructure of each mode.

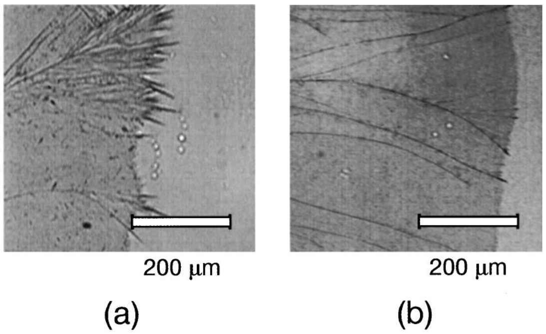

FIG. 13. Mode nucleation in the *DE* transition. (a) Nucleation of mode *D* from mode *E*. This frame shows two domains of mode *D* nucleating from a smooth mode-*E* front following a decrease in undercooling. The mode-*D* needles have grown ahead of the mode-*E* front, allowing them to spread laterally via a branching process. (b) Transition from mode *E* to mode *D*. The mode-*E* front, which becomes established at undercoolings well below the transition point, completes the transition process by burying mode-*D* needles as they curve away from the growth direction. The dark fibers in the solid region behind the front are mode-*D* fibers that have already been buried.

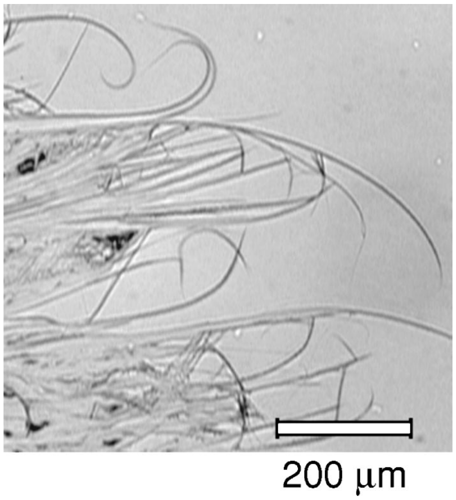

FIG. 14. Mode *D* at small undercooling. The structure resembles the image of mode *D* in Fig. 1, mode *D*, but with increased roughness. Note the curled tips which propagate with constant shape as the fibers lengthen and the broken curl at the center of the image.

We next consider a simple lattice model [29] that shows the consequences of the scenario described above, in the context of a spatially extended system. Consider a square lattice where each cell can be in the smectic state or in either of two solid morphologies (corresponding to modes *C* and *D* for the purposes of this discussion). The initial conditions are a column of cells in mode *D*, with everywhere else smectic. At each time step, smectic sites adjacent to solid sites can be converted into a solid phase. If the solid is mode *C*, the smectic solidifies as mode *C* with probability P_C and to mode *D* with probability P_S (*S* for ''switch''). The probability of remaining in the smectic phase is then $1 - P_C - P_S$. Similarly, smectic sites bordering a mode-*D* cell themselves become mode *D* with probability P_D and switch morphologies with probability P_S. We typically used values of $P_C \sim P_D \sim 0.2$ and $P_S = 0.001$.

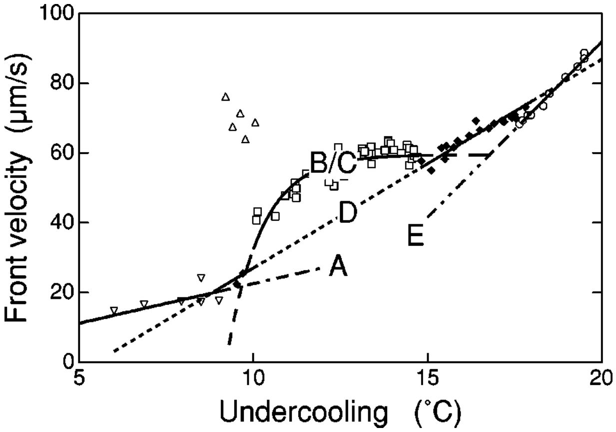

FIG. 15. Mode *D* reentrance. Mode *D* has been observed in two undercooling regions: between modes *C* and *E*, and in a small range near where mode *B*′ is normally observed. For modes *B*/*C*, *D*, and *E*, mode selection seems to follow the ''fastest mode wins'' rule. The smooth lines are meant as a guide to the eye only.

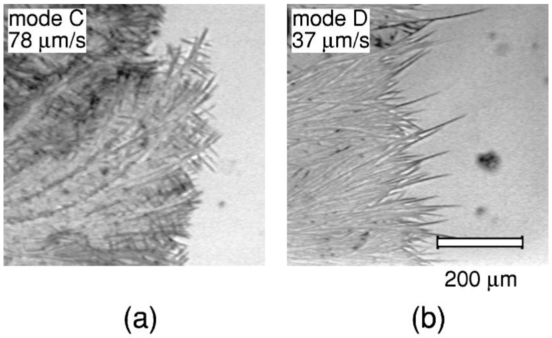

FIG. 16. Growth morphologies in directional solidification. (a) mode *C*. (b) Mode *D*. These experiments were performed with an imposed temperature gradient of 60 °C/cm. Note that the velocities indicated do not agree well with the corresponding modes in free growth, perhaps due to the imposed gradient.

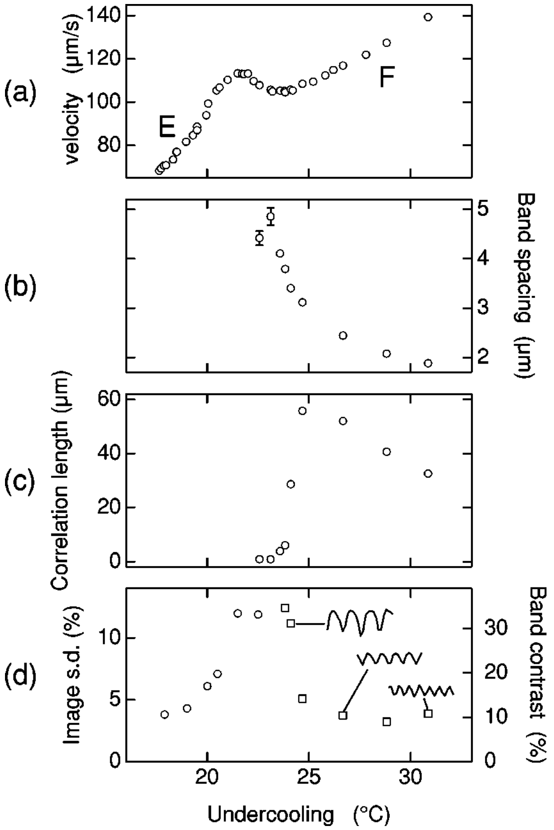

FIG. 17. The *EF* transition. (a) Growth velocity curve for modes *E* and *F*. (b) Band spacing as a function of undercooling for mode *F*. (c) Correlation length of the bands. (d) Measures of the optical contrast. The circles on the left indicate the standard deviation in image intensity for the unbanded mode *E*. The right-hand side shows the average band amplitude in mode *F*. The insets show the evolution of the band profile as a function of undercooling.

This model, though simple, captures a number of features of kinetics-limited growth: it is purely *local*, can generate overhangs, and produces roughness, but does not produce the shape instabilities of the diffusive regime. The key feature is that the front has the ability to hop between two growth modes. When the growth probability (which is proportional to the front velocity) of mode *C* is less than that of mode *D* (i.e., $P_C < P_D$), domains of *C* may nucleate but then die away. For $P_C > P_D$, an initial domain of mode *D* quickly converts to *C*. Examples are shown in Fig. 12. Thus, the velocity curve can remain continuous experimentally — an arbitrarily small velocity difference will allow the faster mode to take over.

The *DE* transition (near $\Delta T = 8$ °C in Fig. 3) shows similar behavior. In this case, some overlap of the two modes is seen. As with the *CD* transition, mode *D* nucleates from a mode-*E* front when the undercooling is reduced [see Fig. 13(a)], signalling a first-order transition. However, the reverse process is more difficult to understand in this context. As shown in Fig. 13(b), mode *E* forms domains throughout the sample long before mode *D* disappears. The needles of mode *D* are buried by the mode-*E* front when they curve away from the direction normal to the mode-*E* front. It appears that the tip velocity of the mode-*D* *needles* remains at least as fast as the average velocity of the mode-*E* front during this process. However, the average *front velocity* for mode *D* becomes less than that of mode *E*. The difference in slope between the average front velocities for modes *D* and *E* suggests that mode *E* would likely take over eventually as the undercooling is increased, even in the absence of curvature in the mode-*D* needles — the effect of this curvature (which may be caused by viscous flow induced by the density difference between the solid and smectic phases) may simply shift the transition point.

The sudden changes in growth morphology and double-valued velocity curve (in the regions where two modes coexist) indicate that *C*, *D*, and *E* represent distinct growth modes, each with a separate dependence of velocity and structure on undercooling, rather than a single growth mechanism with a strong dependence on undercooling. Further evidence is provided by the reentrance of mode *D* at small undercoolings. Near an undercooling of 10 °C, a mode with a slow front velocity is occasionally seen rather than the fast growing mode B' (see Fig. 14). These fronts are similar to the the one shown in Fig. 1, mode *D*, but with a much larger roughness. This roughness makes quantitative comparison difficult, but is consistent with the observation that the mode-*D* roughness increased with decreasing undercooling. As shown in Fig. 15, the position of this mode in a v versus ΔT plot falls near the mode-*D* curve extrapolated to low undercooling.

An interesting feature of the small-undercooling incarnation of mode *D* is that the needle tips are often curled through $>180°$ (note Fig. 14). These curls maintain a nearly constant shape as the front grows. In order to maintain a constant length, the tips must uncurl as new material is added and the needles lengthen. This suggests that the shape represents a balance between stress caused by fluid inflow (caused by the density change on solidification) and the elastic energy of the needle, which increases as the needle thickens. The result is that only a short length near the tip is thin enough to remain bent at any time. The importance of mechanical motion in the solid is highlighted by the fact that the needles frequently break when they grow against neighboring fibers. This increases the number of needle crystals and may be important in the propagation of mode *D*.

The sharp transitions between modes *C*–*E* were also seen in directional solidification experiments (Fig. 16). In direc-

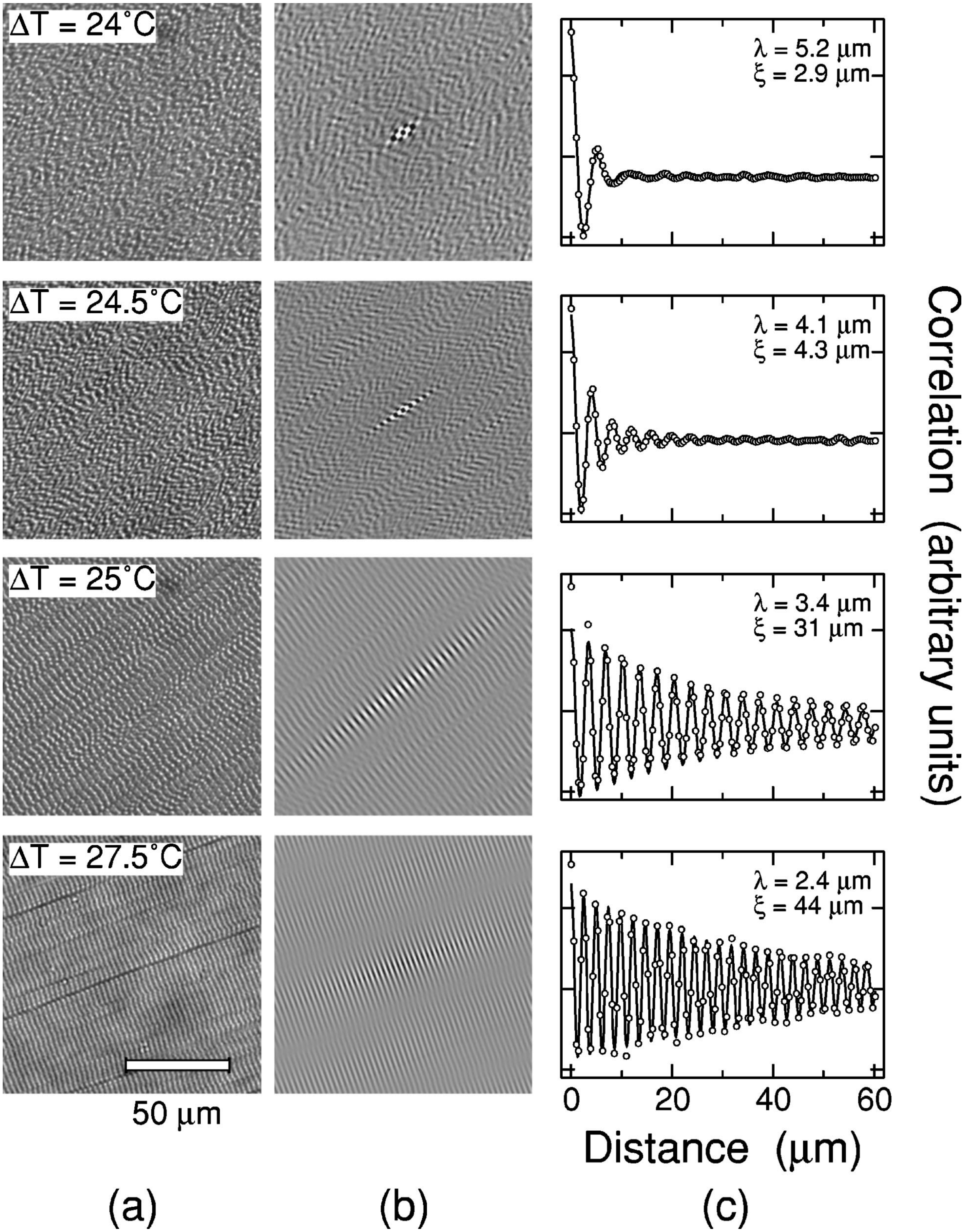

FIG. 18. Measurement of the correlation length. (a) Images of the banded morphology at various undercoolings. (b) Autocorrelation images corresponding to (a). (c) Cross sections along the growth direction (normal to the bands) of the autocorrelation images shown in (b). Each is fit to a cosine function (with wavelength denoted λ) multiplied by a decaying exponential (decay length, ξ) plus a small quadratic baseline.

tional solidification, an initially molten sample is moved at constant velocity through a temperature gradient such that the resulting solidification front is stationary in the frame of the microscope. In this case, the front velocity, rather than the undercooling, is the control parameter, providing an alternative view of mode transitions. The selection rule, which has been seen by other authors [30], becomes the selection of the mode stable at the smallest undercooling (with fixed velocity). Due to the imposed temperature gradient, this mode will then lie at a point ahead of any front at a larger undercooling, effectively choking it off.

Each case of a first-order transition with a continuous velocity curve seen here — the B/C to D transition, the D to E transition, and the transition between mode B/C and the small undercooling version of mode D — is consistent with the ''fastest mode wins rule.'' This is indicated by the smooth lines drawn schematically in Fig. 15. Both the CD and DE transitions are accompanied by increases in the slope of the velocity versus undercooling curve. Thus, extrapolating the mode-D curve into either the mode-C or mode-E regimes would predict a front velocity smaller than that of mode C or mode E, respectively, at the same undercooling. The sharp decrease in front velocity for mode B/C at small undercoolings allows mode D, whose velocity decreases less rapidly with decreasing ΔT, to again become dynamically stable with respect to mode B/C.

VI. A SECOND-ORDER TRANSITION

We have also studied the transition between modes E and F. Note that unlike modes A–D, the mode E and F fronts are compact, indicating that thermal diffusion is likely not the dominant mechanism controlling these morphologies. Mode E is first observed at an undercooling of $\Delta T = 18\,^\circ\mathrm{C}$. Using values of $L \approx 120$ J/g and $c \approx 2$ J/g °C, measured by differential scanning calorimetry, we see that thermal diffusion is no longer expected to be important at an undercooling of $L/c = 60\,^\circ\mathrm{C}$. It may be that, as mentioned earlier, our sample geometry allows access to the kinetic regime at smaller undercoolings. However, there is no *a priori* reason to expect a sharp transition precisely at L/c — the transition to a mode that does not show the characteristics of diffusion-limited growth merely indicates the dominance of another mechanism.

We can identify these modes E and F as normal and banded spherulites, respectively, which are typical of kinetics-limited growth in deeply undercooled viscous melts [23,31]. As details of this study will be published elsewhere [32], only results pertaining to the transition itself will be discussed here.

Neither the velocity curve nor its derivative is discontinuous in the vicinity of the EF transition. The curve does show a complicated structure with a local maximum and minimum as the undercooling is increased. The growth front remains smooth through the transition, with individual crystals too small to image microscopically, so front roughness is not a useful indicator of the transition. Therefore, we have used other quantities, plotted along with the velocity in Fig. 17, to study the transition.

The bands in mode F can be described by their average spacing, Fig. 17(b), and correlation length (measured normal to the direction of the bands), Fig. 17(c), as determined from cross sections of the autocorrelation function (see Fig. 18). In addition, we plot the band amplitude, as measured from optical contrast on the right-hand side of Fig. 17(d). None of these measures can be easily extended to the nonbanded-mode E; instead, we plot the standard deviation of the image intensity on the left side of Fig. 17(d).

The sharp variations in structure point to a sharp transition between modes E and F. Measures of structure disorder — the intensity fluctuations on the mode-E side and the vanishing correlation length on the mode-F side — show the increasing importance of fluctuations as the transition is approached. These observations, along with the smooth, nonhysteretic velocity curve, identify the transition as second order.

The classification of this second-order transition remains elusive. The sudden change in correlation length is consistent with an order-disorder transition [33], but the band contrast does not vanish, as would be expected for such a transition. Alternatively, the diverging wavelength and cusp-like intensity traces suggest a continuous nucleation transition [34]. Near such transitions, domain sizes diverge logarithmically and domains are separated by narrow twist walls. However, the sudden decrease in correlation length near the transition does not fit this scheme.

These macroscopic measurements of spherulitic growth have not addressed the problem of the mechanism responsible for banded growth. The banding mechanism has remained one of the outstanding problems of crystal growth, despite nearly a century of observations. Bands have been associated with a rotation (about the radial direction) of the optic axis of the microcrystals comprising the spherulite [23,35]. However, the origin of this rotation and the cause of large domains of correlated bands continue to be debated. The observation that the transition from unbanded to banded spherulitic growth is a second-order, sharp transition may be important for an eventual understanding of the banding mechanism.

VII. CONCLUSIONS

In conclusion, we have studied transitions between solidification morphologies in the liquid crystalline material 10 OCB as the undercooling is varied. Careful measurements of the velocity versus undercooling curve coupled to quantitative measurements of the macroscopic structure of the resulting solid have allowed us to identify sharp transitions in both the diffusion- and kinetics-limited solidification regimes.

Two of the transitions (AB' and $B'A$) exhibit a jump in both velocity and structure, as expected for first order morphology transitions. In such cases, a ''fastest-mode-wins'' rule cannot apply, as varying the undercooling through the transition in one direction causes a sudden increase in velocity, but causes a velocity *decrease* in the other direction. These transitions, then, must involve other mechanisms, perhaps related to the front structure.

The velocity curve, but not its derivative, is continuous at the transitions between modes B/C, D, and E. Here, discontinuities in structure, signalled by sudden changes in quantities such as the front roughness, show that these, too, are first-order transitions. Each of the transitions in this series favors the fastest-growing mode. The existence of a transition between two modes at precisely the undercooling where their extrapolated velocity curves cross provides strong evidence that for these transitions the selection principle is a function of the average front velocity alone. Because the fastest-mode-wins rule does not apply to strongly first-order transitions (since these cannot be a function of the average front velocity), it is unclear whether or not our results for the

CE and DE transitions are typical of weakly first-order transitions. We remind the reader that in at least one known transition, the rule fails [8].

Finally, we have shown the transition between unbanded and banded spherulitic growth (modes E and F, respectively) in this material to be analagous to a second-order transition. To our knowledge, this is the first example of a true second-order morphology transition. Although the precise nature of this transition remains unknown (as does the banding mechanism itself), this observation may be important for future studies of banded growth.

ACKNOWLEDGMENTS

This work was funded by NSERC (Canada).

---

[1] W. W. Mullins and R. F. Sekerka, J. Appl. Phys. **34**, 323 (1963); W. W. Mullins and R. F. Sekerka, *ibid.* **35**, 444 (1964).

[2] G. P. Ivantsov, Dokl. Akad. Nauk SSSR **58**, 567 (1947), [English translation: G. P. Ivantsov, in *Dynamics of Curved Fronts*, edited by P. Pelcé (Academic Press, New York, 1998), pp. 243–246.

[3] J. D. Hoffman, Polymer **24**, 3 (1983).

[4] J. Lipton, W. Kurz, and R. Trivedi, Acta Metall. **35**, 957 (1987).

[5] D. Grier, E. Ben-Jacob, R. Clarke, and L. M. Sander, Phys. Rev. Lett. **56**, 1264 (1986).

[6] E. Ben-Jacob, P. Garik, T. Mueller, and D. Grier, Phys. Rev. A **38**, 1370 (1988); E. Ben-Jacob and P. Garik, Nature (London) **343**, 523 (1990); O. Shochet and E. Ben-Jacob, Phys. Rev. E **48**, R4168 (1993).

[7] J. S. Langer, Science **243**, 1150 (1989).

[8] R. Willnecker, D. M. Herlach, and B. Feuerbacher, Phys. Rev. Lett. **62**, 2707 (1989).

[9] K. Eckler, R. F. Cochrane, D. M. Herlach, B. Feuerbacher, and M. Jurisch, Phys. Rev. B **45**, 5019 (1992).

[10] Y. Saito and H. Müller-Krumbhaar, Phys. Rev. Lett. **74**, 4325 (1995).

[11] E. A. Brener and D. E. Temkin, Zh. Éksp. Teor. Fiz. **109**, 1038 (1996) [JETP **82**, 559 (1996)]; E. Brener, H. Müller-Krumbhaar, and D. Temkin, Phys. Rev. E **54**, 2714 (1996).

[12] E. Ben-Jacob, R. Godbey, N. D. Goldenfeld, J. Koplik, H. Levine, T. Mueller, and L. M. Sander, Phys. Rev. Lett. **55**, 1315 (1985); Y. Sawada, A. Dougherty, and J. P. Gollub, *ibid.* **56**, 1260 (1986); V. Horváth, T. Vicsek, and J. Kertész, Phys. Rev. A **35**, 2353 (1987); E. Ben-Jacob and P. Garik, Physica D **38**, 16 (1989); O. Shochet, Klaus Kassner, E. Ben-Jacob, S. G. Lipson, and H. Müller-Krumbhaar, Physica A **181**, 136 (1992).

[13] M. C. Cross and P. C. Hohenberg, Rev. Mod. Phys. **65**, 851 (1993) (see especially pp. 1077–1078).

[14] J. L. Hutter and J. Bechhoefer, Phys. Rev. Lett. **79**, 4022 (1997).

[15] BDH Limited, Broom Road, Poole, BH12 4NN, England. 10 OCB exists in a smectic A phase in the range 59.5–84 °C. Below this range, its equilibrium form is a solid, at higher temperatures, it is an isotropic liquid.

[16] John Bechhoefer, in *Spatio-Temporal Patterns in Nonequilibrium Complex Systems*, Santa Fe Institute: Studies in the Sciences of Complexity, Vol. 21, edited by P. E. Cladis and P. Palffy-Muhoray (Addison-Wesley, Reading, Massachusetts, 1994), pp. 107–122.

[17] ZLI 2510, E. Merck, Darmstadt, Germany.

[18] HS1-i Microscope Hot Stage and Temperature Controller, Instec, Inc., Boulder, CO 80306.

[19] Olympus BH-2, Olympus Optical Company, Lmt., Tokyo, Japan.

[20] Pulnix TM-7CN, Pulnix America, Inc., Sunnyvale, CA 94086.

[21] Scion LG-3, Scion Corporation, Frederick, MD 21701.

[22] Canon 108mm, 1–2.5× macro lens.

[23] P. J. Phillips, in *Handbook of Crystal Growth*, Vol. 2, edited by D. T. J. Hurle (Elsevier, Amsterdam, 1993), Chap. 18.

[24] Image processing was performed using NIH Image, v. 1.61, National Institute of Health, Division of Computer Research and Technology, USA.

[25] We assume in the following that these modes are governed by thermal, rather than impurity, diffusion. The measured melting range of the smectic A phase (it was difficult to accurately measure the melting range of the multidomain solid phase) is $<0.1\,°\mathrm{C}$, indicating a low impurity concentration. Moreover, addition of 2% C_2Cl_6 to the samples produced no change in either growth morphologies or transition temperatures of the solid phase, indicating little sensitivity to the presence of impurities.

[26] This estimate derives from modeling the flat interface of thickness d as a cylindrical heat source of circumference d moving at velocity v through a uniform infinite medium of thermal diffusivity D. The indicated correction follows for $vd/D \ll 1$. See J.-C. Geminard, thesis (l'Université Claude Bernard, Lyon, France, 1994) and J. L. Hutter, thesis (Simon Fraser University, Burnaby, Canada, 1997).

[27] The fractal dimension was measured using a NIH Image macro written by Tom Smith, National Institute of Health, Bethesda, MD.

[28] B' was identified as a distinct mode after modes A–F had been defined. We continue to use this label for consistency with earlier publications.

[29] This model is a variant of one discussed in Ref. [10] and is discussed in Ref. [14].

[30] W. Kurz and P. Gilgien, Mater. Sci. Eng., A **178**, 171 (1994).

[31] G. Ryschenkow and G. Faivre, J. Cryst. Growth **87**, 221 (1988); B. Miao, D. O. Northwood, W. Bian, K. Fang, and M. H. Fan, J. Mater. Sci. **29**, 255 (1994).

[32] J. L. Hutter and J. Bechhoefer (unpublished).

[33] C. N. R. Rao and K. J. Rao, *Phase Transitions in Solids* (McGraw-Hill, London, 1978), pp. 120–133.

[34] An example of a continuous nucleation transition is the unwinding of a cholesteric helix by a magnetic field that is transverse to the pitch axis. See P. G. de Gennes and J. Prost, *The Physics of Liquid Crystals* (Clarendon Press, Oxford, 1993), pp. 286–293.

[35] A. Keller, J. Polym. Sci. **17**, 291 (1955).